Applied Catalysis B: Environmental 321 (2023) 122030

Contents lists available at ScienceDirect

Applied Catalysis B: Environmental

journal homepage: www.elsevier.com/locate/apcatb

# Ultralight conductive $IrO_2$ nanostructured textile enables highly efficient hydrogen and oxygen evolution reaction: Importance of catalyst layer sheet resistance

Shougo Higashi *, Atsushi Beniya

*Toyota Central R&D Laboratories, Inc., 41-1 Nagakute, Aichi 480-1192, Japan*

ARTICLE INFO

*Keywords:*
Clean hydrogen
Electrolysis
Nanostructured textiles
Iridium catalysis
Hydrogen and oxygen evolution

ABSTRACT

Large-scale deployment of polymer electrolyte membrane water electrolysis, which is a promising technology for green hydrogen production, requires significant reduction of Ir in catalyst layer due to its high material cost. However, as the Ir amount in the catalyst layer decreases, number of electrically-isolated-inactive catalysts increases, resulting in poor performance. Here we show that the nanostructured textiles essentially avoids the formation of such inactive catalysts, enables unprecedented long-term hydrogen evolution with ultralow Ir mass loadings at high rates. We reveal that achieved high performance is derived from the low resistivity of prepared nanostructured textile which have a unique porous, three-dimensional structure. We also show that the nanostructured textiles facilitate simple catalyst-coated membrane production, which does not require liquid-phase processes or produce chemical waste. The method we developed can also be applied to a variety of zero-gap electrochemical conversion cells that require a high-rate catalytic reactions with small amounts of catalyst.

## 1. Introduction

Hydrogen is a vital element used in various industries, increasingly important towards zero emission society. Polymer electrolyte membrane water electrolysis (PEMWE) produces high-purity hydrogen using pure water and electricity (Eq. (1)), and is considered one of the promising methods for green hydrogen production [1–4].

$$2\ H_2O \rightarrow 2\ H_2 + O_2 \tag{1}$$

To produce hydrogen at a low-operating voltage and high rate, PEMWE systems employ state-of-the-art catalyst-coated membranes (CCMs) [5–7]. CCMs are fabricated from a single PEM sheet coated on both sides with catalysts that promote the hydrogen evolution reaction (HER) and oxygen evolution reaction (OER) (Fig. 1a). Perfluorinated sulfonic acid (PFSA) ionomer-based, cation-exchange membranes (CEMs), such as Nafion, are often used as PEMs in CCMs, but owing to the acidic nature of PFSA, Pt and $IrO_2$ are currently the only practical options for use as durable HER and OER catalysts, respectively, in PEMWE. However, high Ir loading (>1 $mg_{\text{-Ir}}\ cm^{-2}$) is currently required to ensure stable, long-term operation of CEM-based PEMWE processes [8] and it is a substantial cost driver for large scale deployments of PEMWE [9–11].

Catalyst layers are conventionally prepared on PEMs through several steps; generally, synthesis of catalyst followed by preparation of a catalyst ink, comprising synthesized nanocatalysts and a small amount of Nafion solution as a glue [7]. It is splay coated on porous transport layer (PTL) or drop-casted onto a Teflon sheet and transferred onto PEM by a decal process similar to that used to fabricate fuel-cell metal electrode assemblies (Fig. S1a). Unfortunately, this process often leads to nanocatalyst agglomeration as more than 0.5 $mg_{\text{-Ir}}\ cm^{-2}$ is required to achieve a uniform catalyst layer.

At levels below 0.5 $mg_{\text{-Ir}}\ cm^{-2}$, the catalyst layer becomes inhomogeneous due to agglomeration during conventional catalyst layer preparation and the quantity of electrically-isolated inactive catalysts increases. resulting in poor PEMWE performance [12,13]. Such isolation is not problematic in thermochemical catalysis, such as environmental catalysts for automotive application [14,15]; however, it is fatal in electrochemical reactions because it requires electron transfer over relatively long distances between nanocatalyst particles, and from nanocatalyst to current collector. One way for preventing the isolation is the introduction of a conductive support (such as Ti and Pt nanoparticles) that is stable under harsh anodic conditions. This direction has been explored and number of literature confirmed performance

* Corresponding author.
*E-mail address:* shigashi@mosk.tytlabs.co.jp (S. Higashi).

https://doi.org/10.1016/j.apcatb.2022.122030
Received 6 June 2022; Received in revised form 27 August 2022; Accepted 27 September 2022
Available online 4 October 2022
0926-3373/© 2022 The Authors. Published by Elsevier B.V. This is an open access article under the CC BY-NC-ND license (http://creativecommons.org/licenses/by-nc-nd/4.0/).

improvement [16–18]. For instance, micro-sized Ti particles added to a catalyst ink improved both the dispersity of the catalyst and the electrical conductivity of the resultant catalyst layer (0.12 $mg_{-Ir}$ $cm^{-2}$), providing better performance and a cell voltage of only 1.73 V at 1 A $cm^{-2}$ and 80 °C [19]. $IrO_x$-nanoparticle-hybridized $IrO_x$ nanofibers (0.2 $mg_{-Ir}$ $cm^{-2}$) has performed similar to advanced PEMWE cells with catalyst loadings ≥ ~1.0 $mg_{-Ir}cm^{-2}$ [12]. In another study, electrochemically co-deposited Pt and $IrO_2$ (0.16 $mg_{-Ir}$ $cm^{-2}$, 0.27 $mg_{-Pt}$ $cm^{-2}$) on a gas diffusion layer (GDL) produced only 1.61 V at 1 A $cm^{-2}$ and 80 ℃ [16]. As far as we know, this performance is among the best reported for catalyst layers with low Ir mass loadings, but long-term stability for over hundreds of hours is not yet known. Another way is the use of pre-prepared porous, thin-film made of $IrO_2$, such as $IrO_2$-nanostructured thin films (NSTFs, the 3 M Company). The film is prepared by dry processes in advance and transferred onto PEM by decal. High-performance PEMWE has been realized with Ir mass loadings of only ~0.25 $mg_{-Ir}$ $cm^{-2}$ using $IrO_2$-NSTFs. However, this pre-prepared thin-film catalyst causes an abrupt increase in the cell operating voltage when Ir loadings decreases below ~0.25 $mg_{-Ir}$ $cm^{-2}$. The reason for this abrupt voltage increase are not yet known [20,21]. PGM free [22] catalysts and advanced low Ir loading core-shells [23] and alloys [24–28] have been studied in beaker type half-cells, that could reduce dependence on precious metals are also being investigated, but further technological maturity is needed before they can be put to practical use.

In this study, we propose using ultralight conductive $IrO_2$ nanostructured textiles made solely of $IrO_2$ as a catalyst layer of PEMWE as a solution for avoiding the formation of electrically isolated inactive catalysts. we first show that preparing freestanding $IrO_2$ nanostructured textiles by sputtering $IrO_2$ onto a water-soluble polymer nanofiber result in facile CCM preparation. Then, we demonstrate the lowest operational cell voltages reported thus far using CCMs with $IrO_2$ textiles containing only 0.05–0.3 $mg_{-Ir}$ $cm^{-2}$. We also demonstrate excellent stability over 1400 h with a low full-cell operational voltage of ~1.6 V at 1 A $cm^{-2}$ at 80 °C using a CCM containing only 0.2 $mg_{-Ir}$ $cm^{-2}$. Such high performances were previously only achievable with catalysts containing > ~1.0 $mg_{-Ir}$ $cm^{-2}$. We attribute the obtained performance to low sheet resistance of nanostructured textile revealed by four-probe method and high intrinsic activity.

## 2. Experimental

### 2.1. Preparation of nanostructured textiles

A solution of polyvinylpyrrolidone (PVP, $M_w$ 1,300,000; Aldrich Chemical Company, Inc.) was dissolved in methanol to obtain a concentration of 8 wt%. A 6 mL syringe with an inside tip diameter of 0.5 mm was filled with the prepared solution. A constant voltage of 1 kV $cm^{-1}$ was applied between the tip and the metal-foil collector, with an actual distance of 15 cm between them. The solution feed rate was maintained at 1 mL $h^{-1}$ and the total amount of the feed was 0.012 mL $cm^{-2}$ (the solution was electrospun on a square stainless-steel plate with an area of 5 × 5 $cm^2$). Under these conditions, we fabricated PVP nanofibers with diameters of ~270 nm [29–31].

The $IrO_2$ nanostructured textiles were then prepared by depositing catalysts on the electrospun PVP textiles in a vacuum chamber at a base pressure of ~1.5 × $10^{-3}$ Pa by magnetron radiofrequency (RF) sputtering. For preparation of the $IrO_2$ nanostructured textiles, the pressure was maintained at 10 Pa with a gas flow of 5 % oxygen in Ar during sputtering. The metal loading was calibrated using a quartz crystal microbalance (with INFICON, STM-2 thickness monitor) and its accuracy for determining the Ir mass was cross-checked by inductively coupled plasma mass spectrometry ICP-MS. The Pt nanostructured textiles were

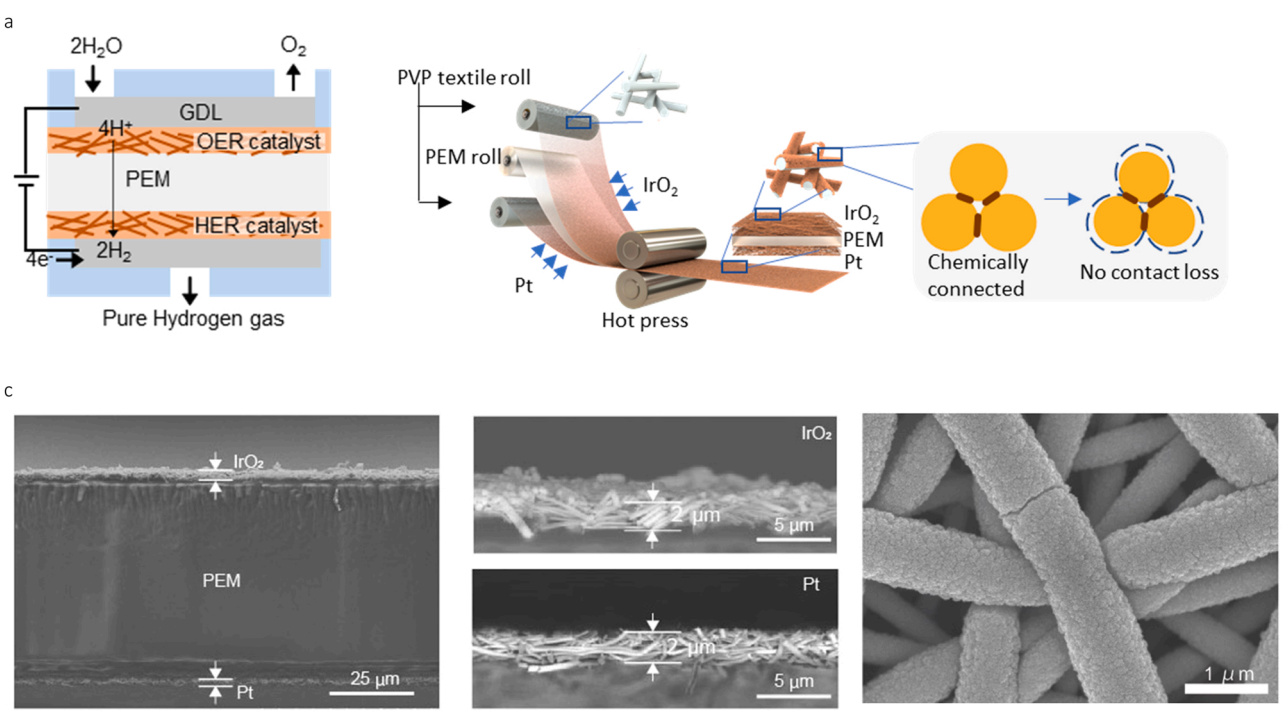


**Fig. 1.** Catalyst-coated membrane with the nanostructured textile. a, Schematic representation of the PEMWE cell. **b,** A sequential roll-to-roll process for fabricating the nanostructured textile CCMs that do not require either a wet chemical route or a labor-intensive preparation process. Conventional catalyst layer preparation requires the wet chemical synthesis of the nanocatalyst, repetition of the centrifugation/cleaning and drying stages, followed by the drop-casting of a catalyst ink consisting of the synthesized nanocatalysts with a low Nafion content, which is intended to glue the nanocatalysts onto the Teflon sheet. Then, the catalyst layer is subsequently hot-pressed and transferred onto PFSA using a decal process (Fig. S1). These processes are not required in the proposed method. **c,** FE-SEM cross-sectional image of the prepared nanostructured textile CCM, showing the porous nanofiber architecture in the catalyst layers. The nanocatalysts which forms textile are chemically connected and even at well-known inevitable Ir dissolution, it maintains electrical paths for catalysis. **d,** SEM of $IrO_2$ nanostuctured textile viewed from $IrO_2$ deposited side.

prepared using a pure Ar gas flow at 10 Pa.

### 2.2. CCM preparation and PEMWE full cell testing

The as-prepared $IrO_2$ and Pt nanostructured textiles on the PVP template were placed on both sides of a PEM (Nafion 212), such that the sputtered side faced the PEM layer. This setup was then sandwiched between Teflon sheets, followed by hot pressing at 120 °C for 10 min at a pressure of 30 MPa (equal to 306 kgf $cm^{-2}$). The corresponding steps were shown in Fig. S1b. The prepared CCM was then installed in the PEM cell, which consist of two Ti plates with holes for flow of water as shown in Fig. S1c. As shown in Fig. S1c, we placed two Pt-coated Ti PTLs (porosity = 56%, thickness = 0.25 mm, Bekaert, product number;2GDL10N-025 BS02PT) as the GDL which is shown in Fig. S2 on both sides of CCM (see Fig. S1c for details of this PEMWE assembly). The Pt-coated Ti-PTLis known to reduce the corrosion of the GDL, resulting in suppressed degradation compared to a non-coated Ti-PTL [32]. The PVP support is water-soluble and so was removed from the PEMWE flow cell system under a flow of water. We note that in the consecutive CCM production, which is shown schematically in Fig. 1b, a PEM roll can be placed between two electrospun PVP-nanofiber-textile rolls. Each PVP-nanofiber-textile roll is coated with OER and HER catalysts by sputtering consecutively to form nanostructured textile catalysts, which are roll-pressed onto both sides of the PEM sheet, and the resulting nanostructured textile CCM is cut into the desired sizes. The prepared CCMs are then placed between the GDLs prior to use.

To compare the performance of the CCM with a conventional catalyst layer prepared from a catalyst ink containing $IrO_2$ nanoparticles, a commercial $IrO_2$ powder (2.65 mg, Alfa Aesar) was dispersed in a solution containing ultrapure water (3.98 mL), a Nafion solution (20 μL, Aldrich, product id: 70160), and isopropanol (1 mL), followed by sonication in an ice bath for 20 min according to a previously reported procedure [33]. The $IrO_2$ catalytic ink was deposited onto the Teflon sheet and dried under ambient conditions for several hours prior to transfer onto the PEM by hot pressing at 120 °C for 10 min at a pressure of 30 MPa. Unless otherwise noted, we employed a Pt nanostructured textile for the HER, and the catalyst mass loading of the Pt textile was maintained at 0.3 mg $cm^{-2}$ for all the tested PEMWE flow cells.

The performance of the PEMWE flow cell was investigated using biologic VSP with a 5 A booster in a temperature-controlled environmental chamber (Espec SH-221), such that the temperature of the cell was maintained at exactly 80 °C. The water flow rate was fixed at 0.2 mL $min^{-1}$. The electrochemical measurements were performed as follows. Initially, the impedance was measured at an open-circuit voltage. Subsequently, a current density of 1 A $cm^{-2}$ was applied for 10 h, then the current density was increased to record the potential evolution curves. Finally, a long-term stability test was carried out at 1 A $cm^{-2}$. To sufficiently supply the water to the catalyst layer, the catalyst layer area for the ink and the textile was kept being ~0.2 $cm^{-2}$ for PEMWE testing but the performance dependence on the areal size of catalyst layer was also investigated as described below.

### 2.3. Sample characterizations

Field-emission scanning electron microscopy (FE-SEM) was carried out using a S5500 FE-SEM instrument (HITACHI High-Technologies). We compared the morphology of textiles before and after the stability text. To view the textile on PVP side, we put the textile into water to thoroughly dissolve the PVP, and then scooped the textile up by a piece of polyimide film so that the PVP side attached to polyimide film. Next, we annealed the textile coated polyimide film at 300°C for 10 min for ensuring the complete removal of residual PVP. Finally, it is placed on a sheet of PEM and hot-pressed in a same way described above for the CCM preparation. This process allows us to clearly view the backside of sputter deposited textile and inside of half-cylindrical nanofibers.

Transmission electron microscopy (TEM) images were acquired on a JEM-ARM200F instrument (JEOL) at an acceleration voltage of 200 kV. X-ray photoelectron spectroscopy (XPS) was performed on a Quantera spectrometer (PHI) using monochromatic Al Kα radiation at an electron take-off angle of 45° and a pass energy of 26 eV. The XPS peak areas were calculated for Ir 4 f in the range of 56–74 eV and were normalized to equality. The O 1 s peak areas were then calculated and normalized using the respective factors from the Ir normalization for each sample. The O 1 s XPS spectra were deconvolved into three peaks as reported in the literature [34–36], using the Voigt function [37]. The minimum values for error estimated by the least-squares method for the XPS spectra were explored at 529–531, 530–532, and 532–534 eV for IrO, OH, and adventitious species, respectively, as has been reported previously [34–36]. The sheet resistance of the prepared catalyst layers was measured by the four-probe method. We employed probes with a distance of 0.1 mm, which is similar to the distance between the Ti GDL fibers used as the current collector in this study (Fig. S2).

### 2.4. Operando XAS with a zero-gap PEMWE cell

The cell employed for operando X-ray absorption spectroscopy (XAS) measurements was composed of two polycarbonate plates; one for each of the OER and HER sides. Each plate possessed two holes, with those on the OER-side plate serving as an inlet for water and an outlet for water and evolved oxygen, while those on the HER-side plate acting as an outlet for hydrogen gas. A parabolic hole, which was tightly sealed by a polyimide film in the OER-side plate was used to secure the path of the fluorescent X-ray. Using this cell, synchrotron radiation was passed through the sealed hole and a slit of a GDL, which also acted as a current collector for the $IrO_2$ catalyst layer, and the transmission and fluorescence XAS were measured simultaneously.

XAS measurements were performed at the beamline BL11S2, Hard X-ray XAFS II, at the Aichi synchrotron radiation center, Japan. XAS was conducted with fluorescence-transmission geometry. During the measurements, XAS spectra for the Pt foil placed behind the sample were simultaneously obtained in transmission mode and were used to align the sample spectra to rule out any systematic energy drifts.

The XANES and extended X-ray absorption fine structure (EXAFS) raw data were processed using the Athena program [38]. Initially, the spectra were normalized, so that the difference between the pre-edge and post-edge regression calculations was equal to one at $E = E_0$ ($E_0$ is the absorption edge (white-line position) determined as the maximum of the first derivative of the XANES spectrum), where the regression equation for the pre-edge ($E < E_0$,) and the post-edge ($E > E_0$) were calculated. Linear equations and third-order polynomials were used as regression equations for the pre-edge and the post-edge, respectively. To extract the EXAFS spectra, the background spectrum extracted from the spline fitting of the post-edge region was subtracted from the normalized spectra and multiplied by $k^3$ to magnify the oscillations. Fourier transforms were performed in the range of k = 2.5–11 $Å^{-1}$ [39].

The $H_2$ gas produced on the cathode side of the PEMWE was passed through a cold trap (immersed in liquid nitrogen for cooling) to remove water, and then introduced into the Quadrupole mass spectrometers (QMS, Pfeiffer Vacuum; PRISMA PRO) chamber through a variable-leak valve to measure the mass spectrum of the produced gas. The mass spectrum before applying the potential to the PEMWE cell was recorded by opening the variable-leak valve until the pressure in the QMS chamber reached $1.7 \times 10^{-7}$ Pa. Subsequently, a current density of 1 A $cm^{-2}$ was applied to the PEMWE cell to record the mass spectrum of the gas produced by water electrolysis. The pressure in the QMS chamber was $1.2 \times 10^{-5}$ Pa. All piping employed in this setup was composed of SUS304 tubes (outer diameter of 1/8). A SUS304 nipple of ICF32 size was used for the cold trap.

## 3. Results and discussions

Fig. 1c shows a typical cross-sectional scanning electron microscopy

(SEM) image of $IrO_2$ and Pt nanostructured textiles on a PEM. The thickness of the catalyst layers was determined to be ~2 μm, and the layers uniformly covered the surface of the PEM. A closer look at the textiles confirmed that their original three-dimensional porous structures were maintained after calendaring. As observed by the top-view SEM image shown in Fig. 1c, the textiles possess open pores with pore diameters ranging from 5 to 10 μm. At a high current density, a large volume of gas can evolve from the catalyst layers that could potentially cause catalyst detachment in the case of tightly-packed catalyst layers produced by conventional catalyst inks. In addition, an increase in the mass-transfer resistance could also result in an increase in the cell operating voltage. The open-pore structures observed for our textiles can therefore suppress such unwanted phenomena, and thus, a low operational voltage can be expected, especially at high current densities.

### 3.1. Performance of PEMWE with nanostructured textile CCM

To investigate the PEMWE performances of these nanostructured textile CCMs, CCMs containing different Ir mass loadings (i.e., 0.05–0.3 $mg_{\text{-Ir}}$ $cm^{-2}$) were prepared. For comparison, control CCMs were prepared using a catalyst ink consisting of a commercial $IrO_2$ and a small amount of Nafion solution (see Figs. S3 and S4 for TEM images of the commercial $IrO_2$ and photographic images of the prepared CCMs, respectively). The potential evolution curves of the control CCM prepared by conventional ink processing with Ir mass loadings of 0.5 and 0.1 mg $cm^{-2}$ and that of a previously reported high-performance CCM [16] are also plotted. This previously reported CCM showed the highest performance for a CCM containing an Ir/Pt catalyst layer prepared on a 250-μm-thick Ti porous transport layer (PTL) by electrodeposition, with a low Ir-mass loading of 0.16 $mg_{\text{-Ir}}$ $cm^{-2}$, along with 0.27 $mg_{\text{-Pt}}$ $cm^{-2}$ Pt. We note that the size of $IrO_2$ nanoparticles grown on the PVP textile was about 1–2 nm (Fig. S7) in diameter while the commercial one used to prepare the catalyst ink was ~25 nm in diameter. As shown in Fig. 2a, the operational cell voltages of our prepared CCMs (even that containing 0.05 $mg_{\text{-Ir}}$ $cm^{-2}$) were suppressed at all the investigated current densities compared to those of the control CCMs. Notably, the operational voltages were < 2 V at the highest current density of 7 A $cm^{-2}$, which, to the best of our knowledge, is the lowest voltage reported to date for CCMs with catalyst amounts as small as those employed in this study. The cell operational voltage of PEMWEs with $IrO_2$ nanostructured textiles increased with decreasing the Ir mass loading, because the total number of active sites also decreases as the mass loading decreases. As expected, there was no increase in abrupt cell voltage when the mass loading decreased below 0.2 $mg_{\text{-Ir}}$ $cm^{-2}$, in contrast to previous observations [40].

Fig. 2b shows a comparison of the changes in PEMWE cell voltages

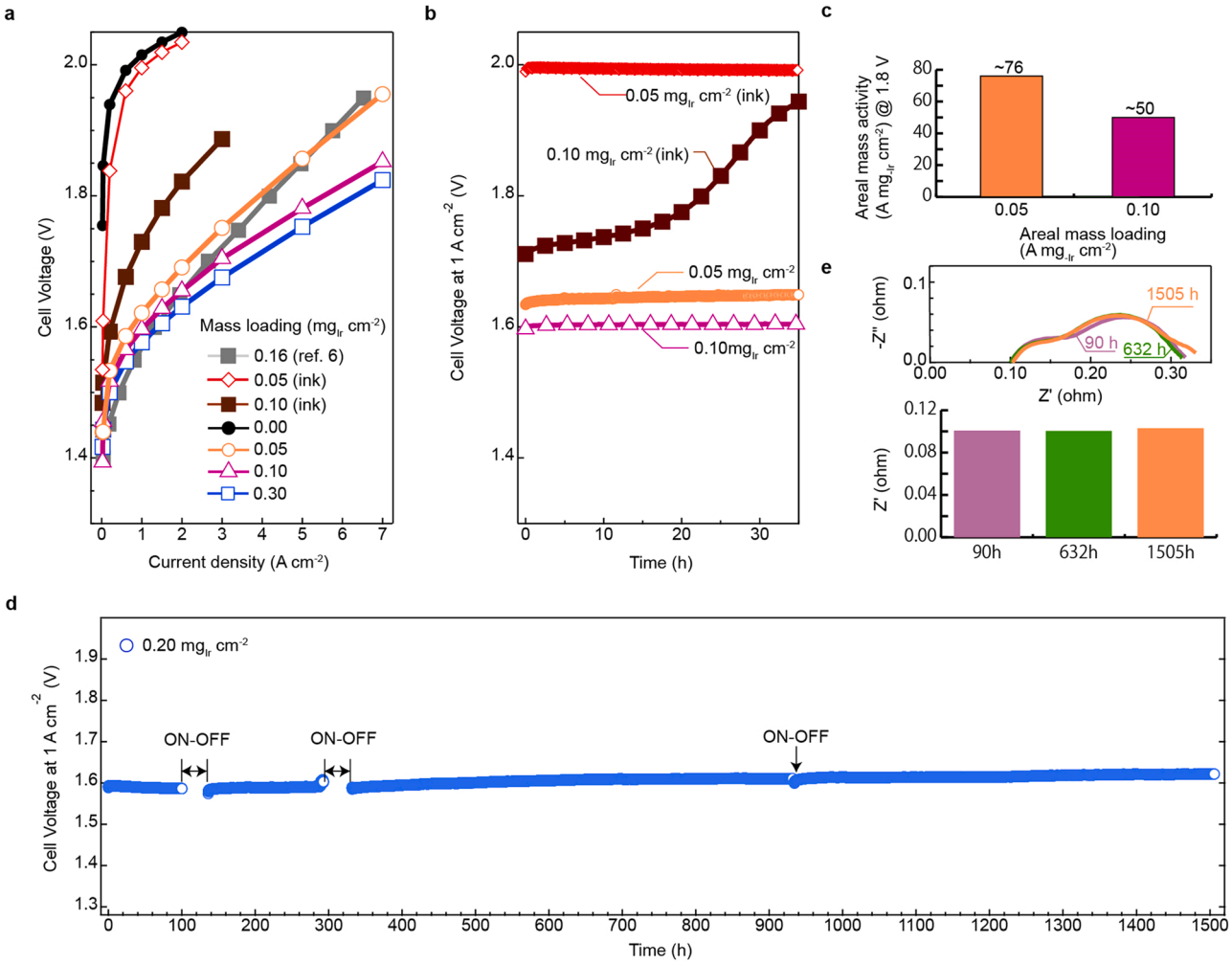


**Fig. 2.** Performance of a PEMWE cell composed of the $IrO_2$ textile CCMs. a, Operational voltage evolution curves of conventional nanoparticles and the textile CCMs at different current densities and different mass loadings. b, Stability test under a current density of 1 A $cm^{-2}$. c, Areal mass activities at 1.8 V for the $IrO_2$ textile containing 0.05 and 0.1 $mg_{\text{-Ir}}$ $cm^{-2}$. d, Long-term stability test under a current density of 1 A $cm^{-2}$ using the $IrO_2$ nanostructured textile, showing stable operation for more than 1400 h. To investigate the effect of the current on/off condition on the performance, we set times when no current was applied, as indicated by ON-OFF in the figure (Fig S5 shows the curves with different areal size of catalyst layers). e, Impedance curves of the PEMWE at different operation times.

under 1 A $cm^{-2}$, which correspond to the $H_2$ evolution rate of 9 mL $min^{-1}$ $cm^{-2}$, over time between the control CCM consisting of conventional nanocatalysts prepared by ink processing, and the PEMWE cells with $IrO_2$-nanostructured textile CCMs. 1 A The CCM prepared by ink processing with an Ir mass loading of 0.05 $mg_{\text{-Ir}}$ $cm^{-2}$ showed similar performance to that of the CCM without $IrO_2$, indicating the catalyst was too small to make good contact with the current collector. The CCM prepared by ink processing with 0.10 $mg_{\text{-Ir}}$ $cm^{-2}$ exhibited an operational voltage of ~1.7 V initially, then displayed a steep increase at approximately 20 h. The increase in the cell voltage observed for the control CCMs can be explained by the formation of isolated catalysts due to the dissolution of Ir, resulting in an increased number of molecules evolving per second at the surviving catalytically active sites, which in turn caused further dissolution of Ir at the sites. Hence, a steep increase in the operating voltage of the cell occurred [41–43]. In contrast, the $IrO_2$ nanostructured textile did not show a significant voltage increase.

In terms of the catalytic activity, the areal activity and mass activity are the two key parameters that are commonly used individually. However, for practical application, especially for the purpose of reducing the total mass loading of catalysts, areal mass activity defined by the current density normalized by areal mass loading at a specific potential (A $mg_{\text{-Ir}}^{-1}$ $cm^{-2}$) is more relevant than conventional specific activity (A $mg_{\text{-Ir}}^{-1}$) and conveniently for comparison among literatures. In this study, we achieved unprecedented high areal mass activities of ~76 and ~50 A$mg_{\text{-Ir}}^{-1}$ $cm^{-2}$ at 1.8 V for the $IrO_2$ textile containing 0.05 and 0.1 $mg_{\text{-Ir}}$ $cm^{-2}$, respectively (Fig. 2c).

The long-term performance of the PEMWE cell containing the textile CCM with an Ir mass loading of 0.2 $mg_{\text{-Ir}}$ $cm^{-2}$ was further investigated under the same current density, but with a longer operation time. As shown in Fig. 2**d**, the PEMWE cell was active for > 1500 h with only a small increase in the operational voltage being detected; such stability has not yet been observed for a CCM with such a low Ir mass loading. During these long-term stability tests, we also investigated how cessation of the CCM function would affect the performance of the PEMWE cell. This was achieved by removing the current after 100 and 300 h, after which the current remained off for several tens of hours; it was also stopped at approximately 950 h for a short period of time. It was found that these intervals without current had no significant impact on the steady-state operation of the PEMWE cell, thereby indicating its potential for use in practical applications. The energy efficiency of the higher heating value (HHV) can be estimated to be 91.4% assuming a voltage of 1.62 V at the end of the measurement (3.88 kWh $m_{H2}^{3}$). We used simple gas-tight cell, made of two Ti plate without serpentine water flow path as described in experimental section, but it maintained similar performance for the larger catalyst layer area of 1 cm x 1 cm squared (Fig. S5a). For 2 cm × 2 cm squared $IrO_2$ and Pt nanostructured catalyst textiles CCM, the PEMWE operational potential was increased as shown in Fig. S5b., which is presumably due to the insufficient water supply.

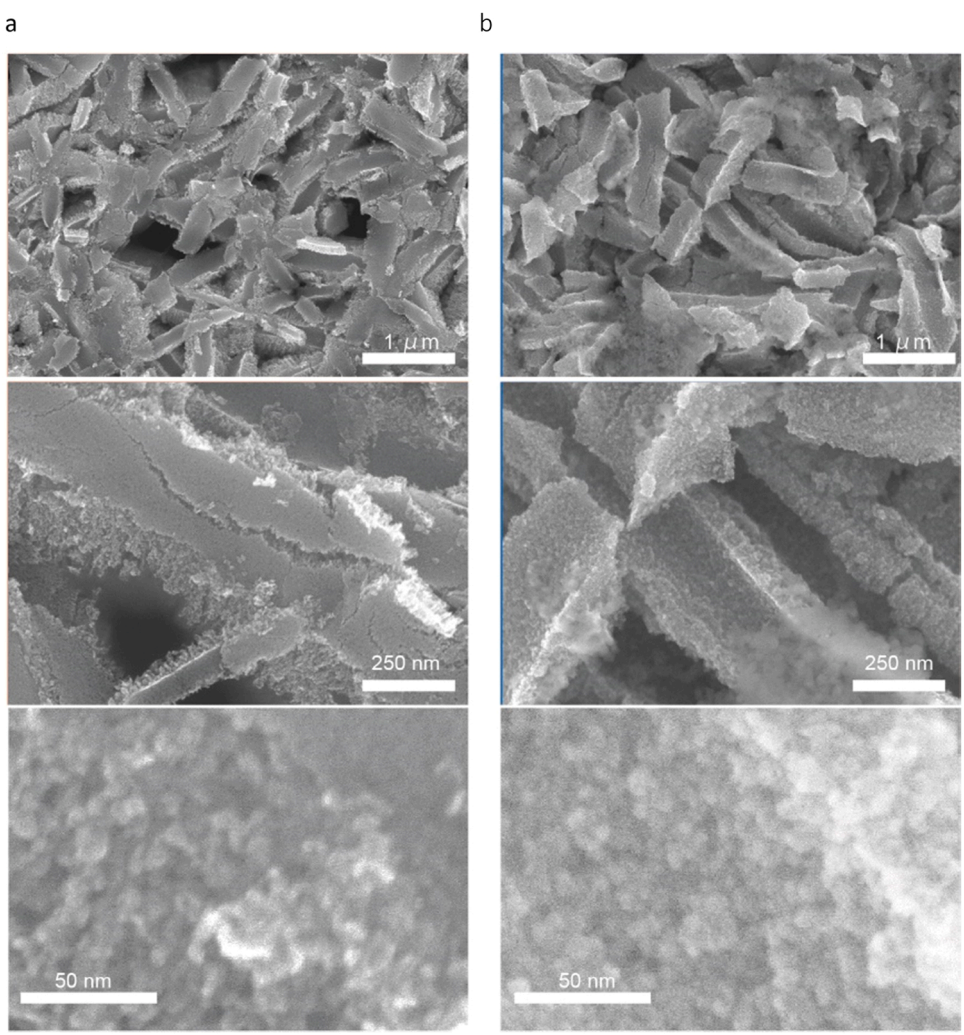


**Fig. 3. a,** SEM image of the $IrO_2$ nanostructured textile with an Ir loading of 0.20 $mg_{\text{-Ir}}$ $cm^{-2}$ viewed from the side with the PVP template nanofiber textile. **b,** The same mass loading textiles after the long-term stability test. Water supply during PEMWE removes the PVP and thus half-cylindrical structure was observed in these images (details in Experimental section).

We expect that appropriate engineering of PEMWE cell would avoid such potential increase.

The impedance was also measured during these tests for operating times of 90, 632, and 1505 h at a current density of 1 A $cm^{-2}$ (Fig. 2e). Two semicircles were observed in the resultant impedance curves, as previously reported [43]; the semicircle at the higher frequency represents the cathodic process, whereas the other denotes the anodic process. We observed a slight decrease in the size of each semicircle with an increase in the operation time of PEMWE. The ohmic resistivity of the PEM, which was read as the point of the higher end of the semicircle that crossed the real axis, was ~0.10 Ω, and remained approximately unchanged. The potential degradation rate was therefore estimated to be 18 μV $h^{-1}$, which is among the lowest values reported for CCMs with such a low Ir mass loading. The observed stable operation indicates that there is no significant morphological change in the textile structure. To confirm if it is true, we compared the morphology of the $IrO_2$ nanostructured textile before and after the long-term stability test in Fig. 3. As expected, the $IrO_2$ nanostructured textile maintained its original half-cylindrical morphology after long-term WE which is in line with the observed stable PEMWE operation. For PEMWE test, we placed nanostructured textile on PEM so that the metal deposited side faced to PEM (see Experimental). PVP is water soluble and thus, the SEM image view the side where PVP nanofiber textile were originally existed, exhibiting a bunch of half-cylindrical $IrO_2$ nanofibers.

As for the surface chemical state, the number of OH groups was not significantly different from that in the pristine textile after the stability test, while a slight shift of the Ir 4 f peak to a higher BE was observed. The result indicates that more O species surround the Ir atoms after the stability test (Fig. S6). To confirm this, we quantified the atomic concentrations of Ir and O from the spectra and found that the textile had a higher atomic concentration of O after the stability test, consistent with the Ir 4 f peak shift.

As previously discussed, it is important to measure the actual amount of gas evolved, especially when claiming record-high efficiency [44]. Thus, to confirm that the gas produced by our PEMWE cells is indeed $H_2$, and to demonstrate that the obtained gas volume matches with the theoretically calculated volume, we applied a current of 2 A to the PEMWE flow cell for 79.4 s, which would typically be expected to produce 20 mL of $H_2$ gas. As shown in Fig. 4, we confirmed that 20 mL of $H_2$ gas was indeed obtained. The produced gas was then further analyzed by quadruple mass spectroscopy (QMS), and only signals corresponding to $H_2$ and $H_2O$ were observed; the latter were present due to the reaction between $H_2$ and the background $O_2$ gas present in the QMS chamber. This suggests that high-purity hydrogen was formed, with no parasitic reactions occurring during PEMWE.

### 3.2. Surface of the $IrO_2$ nanostructured textile

To investigate how the surface of the highly active $IrO_2$ nanostructured textile was terminated, we performed high-resolution transmission electron microscopy (HRTEM) and thoroughly analyzed the frequency of appearance of the surface planes in a statistical manner (Fig. 5**a**). Through this observation, the formation of crystalline rutile $IrO_2$ was confirmed, and {100}, {231}, {121}, and {301} planes were observed on its surface; these do not appear in the equilibrium shape of $IrO_2$ determined by Wulff construction which provides equilibrium shape of materials that has the minimum surface energy (Fig. 5**b**). This simulated $IrO_2$ exposes the (110), which is the most which is the most stable termination [45]. Fig. 5**c** summarizes the surface area of each observed plane of the $IrO_2$ nanostructured textile, which exhibits features that are quite different from those of the Wulff construction. To investigate whether the unique morphology of our prepared $IrO_2$ textile nanoparticles is reproduced and validate our analyses, we prepared a bulk crystal model of rutile $IrO_2$ and cut it into a model whose four surface planes (i.e., {100}, {231}, {121}, and {101}) exhibited frequencies of appearance that were similar to those of the planes observed for our prepared $IrO_2$ nanostructured textile. As a result, the grain-like morphology observed by field-emission scanning electron microscopy (FE-SEM) and TEM was successfully reproduced, as shown in Fig. 5**d**, and successfully validated our analyses. In addition to the appearance of high index facets, a large number of undercoordinated surface Ir atoms were observed since the size of grains was small and it have a large number of edges, which is one of the other unique characters for $IrO_2$ nanostructured textile.

### 3.3. Chemical state analysis by operando XAS

The presence of a large number of D-band holes increases the number of O 2p holes, and the consequential electrophilic nature facilitates nucleophilic acid–base-type O–O bond formation [39,46]. Hence, the greater the number of D-band holes, the higher the catalytic activity, as proposed previously. Thus, to investigate the Ir 5d hole count of our low Ir mass loading $IrO_2$ nanostructured textile CCMs, operando XAS was performed for the $IrO_2$-nanostructured textiles during the PEMWE

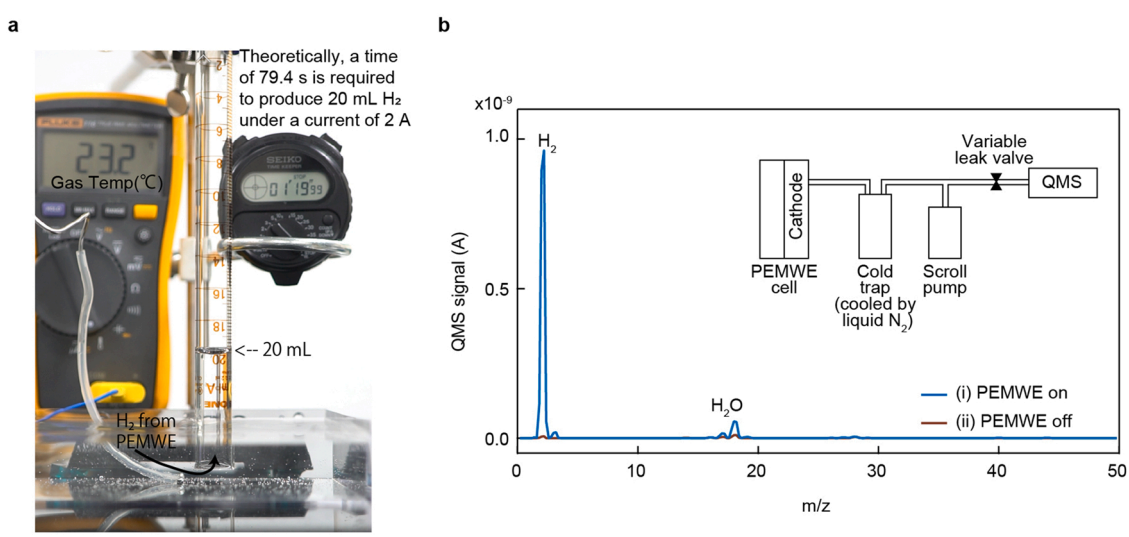


**Fig. 4.** Hydrogen evolution under a constant current. a, Photographic image of 20 mL of hydrogen in a graduated cylinder, which was produced by applying a current of 2 A to the PEM cell for 79.4 s **b**, Mass spectrum of the produced gases before and during the water electrolysis process, confirming the production of high-purity $H_2$. The inset of Fig. 3b shows analysis system for the gases produced from the cathode side of the PEMWE cell.

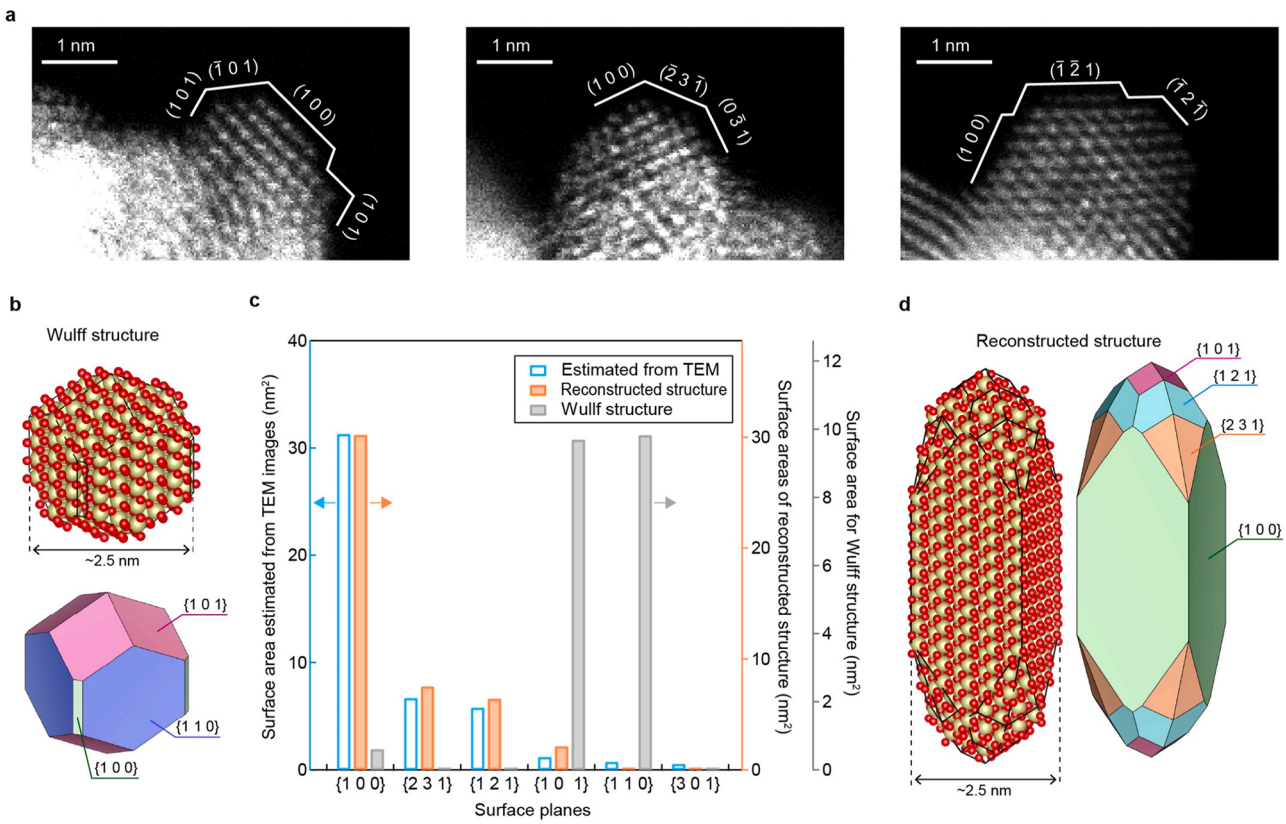


**Fig. 5.** Surface planes on the $IrO_2$ nanostructured textile. a, Typical HAADF-STEM images of the $IrO_2$ catalyst textile surface, showing the topmost surface atom arrangement. b, Equilibrium shape of an $IrO_2$ nanoparticle with a diameter of 2.5 nm as deduced by a Wulff construction c, Distribution of the surface areas estimated from the HAADF-STEM images (white bar graphs outlined by light-blue lines). The orange bars indicate the surface area distribution of the model nanoparticle shown in (b). The gray bars show the distribution of the surface area for the structural model shown in (d), as calculated by a Wulff construction, which differs significantly from the experimentally obtained surface area distribution. d, An $IrO_2$ nanoparticle reproduced by considering the total surface area of each surface plane in (c).

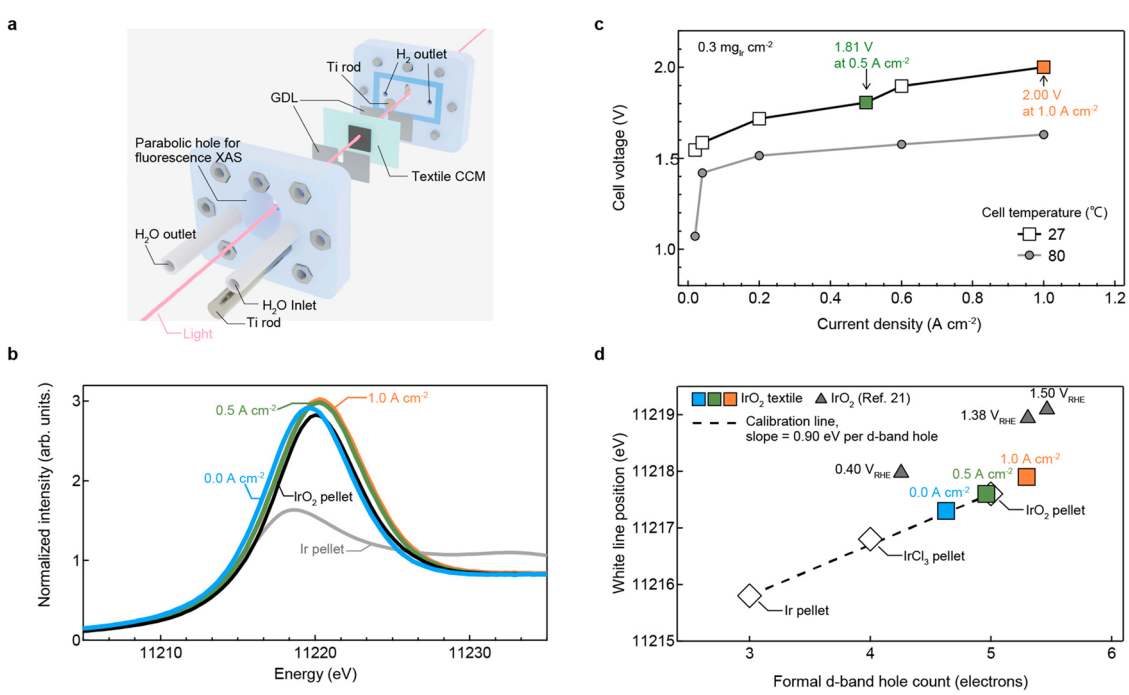


**Fig. 6.** Chemical states characterization by Operand XAS. a, An illustration of the PEMWE flow cell used for the Operand XAS measurements. b, XANES results for the Ir L(III) edge of the $IrO_2$ textile CCM at different current densities, and the corresponding potential evolution curves (c). XAS was carried out at 27 °C. Potential evolution curve of the operand XAS PEMWE cell measured at 80 °C is also shown. d, Formal D-band hole counts at different current densities. A D-band hole count of 5.3 was achieved at 1.0 A $cm^{-2}$, which is close to the value obtained for the intrinsically highly active $IrNiO_x$ catalysts [39].

process. Fig. 6a shows an illustration of the PEMWE cell used for the operando XAS measurements. Fig. 6**b** shows potential evolution curves of this PEMWE cells at different temperatures, and operando XAS performed with 0.5 and 1 A $cm^{-2}$ at ~27 °C. The Ir-L(III) edge of the X-ray absorption near edge structures (XANES) at different current densities indicated in Fig. 6b are shown in Fig. 6c. To estimate the number of D-band holes, the white lines (WLs) of one of the prepared textiles and of Ir, $IrCl_2$, and $IrO_2$ were measured. Without the application of a current, the WL of the prepared textile was located between those of $IrCl_2$ and $IrO_2$. At a current density of 0.5 A $cm^{-2}$ (or 1.81 V), the textile WL shifted slightly toward that of $IrO_2$, while at 1 A $cm^{-2}$, the textile WL shifted to an even higher energy (XAFS spectra of the $IrO_2$ textile at different current densities is shown in Fig. S8). Using the calibration line estimated by the positions of the WLs of the reference materials, i.e., Ir, $IrCl_3$, and $IrO_2$ (0.90 eV per D-band hole, similar to previous results obtained for IrNiOx [39]), we estimated the formal D-band hole count at different applied current densities (Fig. 6d). The change in the number of D-band holes from the non-biased state to the state at 1.0 A $cm^{-2}$ was ~0.6, and the hole count at 1.0 A $cm^{-2}$ reached 5.3, close to the value obtained for $IrNiO_x$ which showed among the highest intrinsic activities reported for half-cell experiments [39]. These results suggest that our $IrO_2$ textile CCM is intrinsically highly active and consistent to the observed highest mass areal activities, which are presumably derived from the unique high-index surface termination observed through HRTEM on which surfaces hold a large number of OH species.

### 3.4. Origin of the high stability of the textile CCMs

Ultralight $IrO_2$-nanostructured textiles enabled long-term stable operation of PEMWE. The achieved high stability is most likely due to the unique interconnected structure which ensured the electric connection between nanocatalysts and the current collector. To confirm that the electrical conductivity of $IrO_2$ nanostructured textiles is indeed higher than that of a conventional catalyst layer, we measured the sheet resistance of the catalyst layers by the four-probe method. As expected, while the sheet resistances of the conventional catalyst layers prepared with ink with Ir mass loadings of 0.05 and 0.10 $mg_{\text{-Ir}}$ $cm^{-2}$ were immeasurably high, the $IrO_2$ nanostructured textile with equivalent mass loadings exhibited smaller sheet resistances of ~9.7 and ~5.8 k ohms per square (kΩ/□), respectively. The insulating property observed in the conventional catalyst layer prepared by ink is consistent to SEM observations which confirmed the aggregation of catalysts (Fig. 7a), whereas interconnected fibrous structure were confirmed on textile CCM as shown in Fig. 7b, suggesting that the high stability obtained derives from an electrically connected textile structure which exhibited low sheet resistance (We note that nanostructured textile consists solely of sputtered materials ($IrO_2$) and does not contain any binder since it is in one piece and connected). The results is in line with the previous study which revealed that the sheet resistance of anode catalyst layer has a significant impact on the distribution of oxygen bubble generation site [47].

Our HRTEM analyses revealed that the few nm nanocatalyst surface forming the textile was terminated by high indexed surfaces. Local surface structure, exposed surface planes, and coordination number of the surface atoms are determining factors of intrinsic catalytic activity [48], and elucidating the atomic-surface structure is the critical task for designing efficient catalyst layers. Through these analyses, we revealed unique surface terminations of our $IrO_2$-textile catalyst and the presence of undercoordinated surface Ir atoms, both of which could contribute to the observed high intrinsic catalytic activity. XAS analyses revealed the unique chemical state of $IrO_2$ nanostructured textiles which has been observed for high active OER catalyst. It is presumably associated to the unique surface structure, however, to directly associate the structure, chemical state, and activity for improving the PEMWE performance, further fundamental experimental and theoretical studies, preferably with a catalyst system that has a well-defined model, are expected.

## 4. Conclusions

We demonstrated high-rate hydrogen production at a low PEMWE operational voltage using CCMs consisting of ultralight catalyst textiles with significantly lower Ir mass loadings (i.e., <1/10) than those of conventional CCMs. The excellent long-term stability was explained by the interconnection of the nanocatalysts in the $IrO_2$ nanostructured

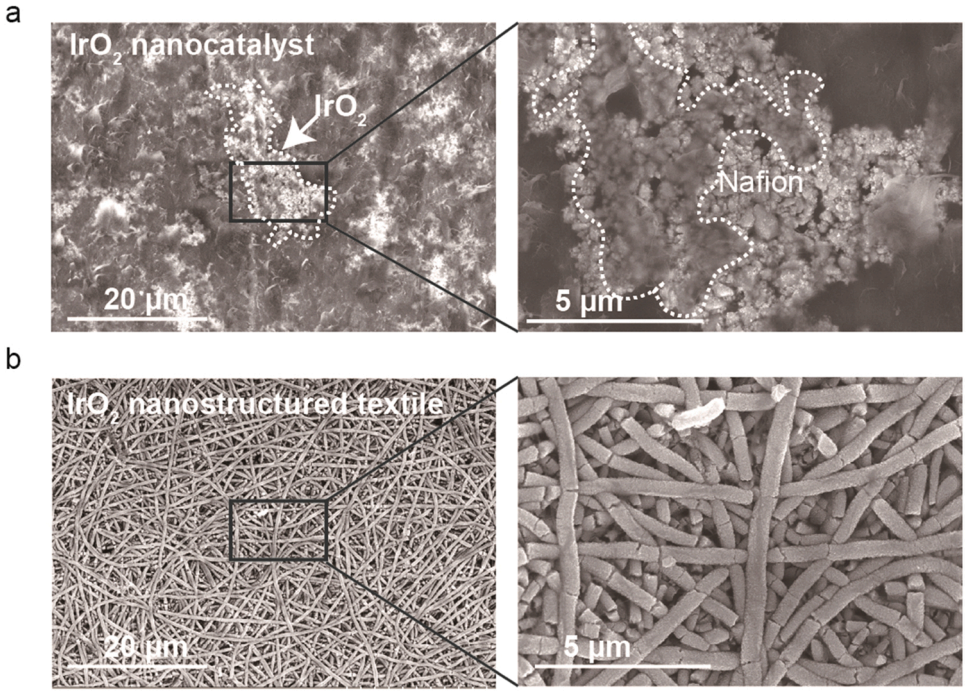


**Fig. 7.** Comparison of SEM images of $IrO_2$ catalyst layer prepared with commercial $IrO_2$ and $IrO_2$ nanostructured textile. a, SEM image of catalyst layer on Nafion 212 made by conventional $IrO_2$ nanoparticles and (**b**) $IrO_2$ nanostructured textile. Mass loading of Ir is 0.1 $mgcm^{-2}$ for both samples.

textiles, which secured the required electrical contact and avoid formation of isolated catalysts. In addition, the highly efficient PEMWE was attributed to the large surface area and porous structure that facilitated mass transfer. Through analysis by operando XAS, we revealed that the $IrO_2$-nanostructured textile possesses a large number of D-band holes and is intrinsically highly active. Moreover, these nanostructured textile CCMs were prepared via a simple but scalable environmentally-friendly method and was easy to be transferred. We expect that this technology will facilitate the preparation of CCMs and will also be applicable to other zero-gap electrochemical conversion cells, including those that use alkaline anion-exchange membranes (AEMs), which are expected to enable the use of non-platinum group metal (PGM) catalysts [22,49]. It is worth noting that OER catalysts with low Ir content have been extensively studied in half-cells, and excellent performances have been reported [26,50,51]; performance evaluation in a PEMWE full cell is awaited. Low conductivity is not problematic in such half-cell experiments, since the nanocatalyst is coated on a conductive metal (or sometimes carbon black is mixed together with catalysts to compensate conductivity, which is not durable under full cell harsh conditions), however, in the full cell evaluation, assuring sufficient conductivity between nanocatalysts and developing a three-dimensional structure for an efficient mass transport will be significant challenges when these catalysts are applied to PEM [52]. The concept and method we developed will fill the large gap between the half and full-cell PEMWE, help resolving these problems, especially at ultralow catalyst mass loadings, thereby contributing to the realization of cost-effective PEMWE.

## CRediT authorship contribution statement

S. H. and A. B. conceived the idea and designed the experiments. A. B. performed the XPS measurements and TEM structural analyses. S. H. measured the sheet resistance of catalyst layer and A. B. performed the XAS measurements and prepared the manuscript.

## Declaration of Competing Interest

The authors declare that they have no known competing financial interests or personal relationships that could have appeared to influence the work reported in this paper.

## Data Availability

Data will be made available on request.

## Acknowledgements

We thank Masahiro Yokoi for designing the PEMWE cell, H. Kato for offering technical assistance during the XAS measurements, Yasutomo Goto for BET measurements and FESEM, Satoru Kosaka for ICP-MS, Naoko Takahashi for XPS. We also thank Hirokazu Nakagawa and Rie Taguchi for their technical assistance.

We acknowledge Toru Asaka for TEM observations and insightful comments on TEM analyses. This work was supported by the Nanotechnology Platform Program of Ministry of Education, Culture, Sports, Science and Technology (MEXT), Japan, grant number JPMXP09S21NI0018.

## Appendix A. Supporting information

Supplementary data associated with this article can be found in the online version at doi:10.1016/j.apcatb.2022.122030.

## References

[1] M. Chatenet, et al., Water electrolysis: from textbook knowledge to the latest scientific strategies and industrial developments, Chem. Soc. Rev. (2022), https://doi.org/10.1039/D0CS01079K.
[2] U. Babic, M. Suermann, F.N. Büchi, L. Gubler, T.J. Schmidt, Critical review—identifying critical gaps for polymer electrolyte water electrolysis development, J. Electrochem. Soc. 164 (2017) F387.
[3] S. Stiber, et al., A high-performance, durable and low-cost proton exchange membrane electrolyser with stainless steel components, Energy Environ. Sci. 15 (2022) 109–122, https://doi.org/10.1039/D1EE02112E.
[4] Z. Chen, et al., Advances in oxygen evolution electrocatalysts for proton exchange membrane water electrolyzers, Adv. Energy Mater. 12 (2022), 2103670, https://doi.org/10.1002/aenm.202103670.
[5] S. Siracusano, N. Van Dijk, E. Payne-Johnson, V. Baglio, A.S. Aricò, Nanosized IrOx and IrRuOx electrocatalysts for the O2 evolution reaction in PEM water electrolysers, Appl. Catal. B: Environ. 164 (2015) 488–495, https://doi.org/10.1016/j.apcatb.2014.09.005.
[6] T. Hrbek, et al., Sputter-etching treatment of proton-exchange membranes: completely dry thin-film approach to low-loading catalyst-coated membranes for water electrolysis, Int. J. Hydrog. Energy 45 (2020) 20776–20786, https://doi.org/10.1016/j.ijhydene.2020.05.245.
[7] Z. Xie, et al., Optimization of catalyst-coated membranes for enhancing performance in proton exchange membrane electrolyzer cells, Int. J. Hydrog. Energy 46 (2021) 1155–1162, https://doi.org/10.1016/j.ijhydene.2020.09.239.
[8] H. Yu, et al., Nano-size IrOx catalyst of high activity and stability in PEM water electrolyzer with ultra-low iridium loading, Appl. Catal. B: Environ. 239 (2018) 133–146, https://doi.org/10.1016/j.apcatb.2018.07.064.
[9] K.E. Ayers, et al., Pathways to ultra-low platinum group metal catalyst loading in proton exchange membrane electrolyzers, Catal. Today 262 (2016) 121–132, https://doi.org/10.1016/j.cattod.2015.10.019.
[10] D. Kulkarni, et al., Elucidating effects of catalyst loadings and porous transport layer morphologies on operation of proton exchange membrane water electrolyzers, Appl. Catal. B: Environ. 308 (2022), 121213, https://doi.org/10.1016/j.apcatb.2022.121213.
[11] M. Bernt, H.A. Gasteiger, Influence of ionomer content in IrO2/TiO2electrodes on PEM water electrolyzer performance, J. Electrochem. Soc. 163 (2016) F3179–F3189, https://doi.org/10.1149/2.0231611jes.
[12] C. Rozain, E. Mayousse, N. Guillet, P. Millet, Influence of iridium oxide loadings on the performance of PEM water electrolysis cells: Part I–Pure IrO2-based anodes, Appl. Catal. B: Environ. 182 (2016) 153–160, https://doi.org/10.1016/j.apcatb.2015.09.013.
[13] M. Bernt, et al., Current challenges in catalyst development for PEM water electrolyzers, Chem. Ing. Tech. 92 (2020) 31–39, https://doi.org/10.1002/cite.201900101.
[14] A. Beniya, S. Higashi, Towards dense single-atom catalysts for future automotive applications, Nat. Catal. 2 (2019) 590–602, https://doi.org/10.1038/s41929-019-0282-y.
[15] A. Beniya, et al., CO oxidation activity of non-reducible oxide-supported mass-selected few-atom Pt single-clusters, Nat. Commun. 11 (2020) 1888, https://doi.org/10.1038/s41467-020-15850-4.
[16] A. Lim, et al., Low-loading $IrO_2$ supported on Pt for catalysis of PEM water electrolysis and regenerative fuel cells, Appl. Catal. B: Environ. 272 (2020), 118955, https://doi.org/10.1016/j.apcatb.2020.118955.
[17] C.V. Pham, et al., IrO2 coated $TiO_2$ core-shell microparticles advance performance of low loading proton exchange membrane water electrolyzers, Appl. Catal. B: Environ. 269 (2020), 118762, https://doi.org/10.1016/j.apcatb.2020.118762.
[18] Y. Jiao, Y. Zheng, M. Jaroniec, S.Z. Qiao, Design of electrocatalysts for oxygen- and hydrogen-involving energy conversion reactions, Chem. Soc. Rev. 44 (2015) 2060–2086, https://doi.org/10.1039/C4CS00470A.
[19] C. Rozain, E. Mayousse, N. Guillet, P. Millet, Influence of iridium oxide loadings on the performance of PEM water electrolysis cells: Part II – advanced oxygen electrodes, Appl. Catal. B: Environ. 182 (2016) 123–131, https://doi.org/10.1016/j.apcatb.2015.09.011.
[20] K.A. Lewinski, D. van der Vliet, S.M. Luopa, NSTF advances for PEM electrolysis - the effect of alloying on activity of NSTF electrolyzer catalysts and performance of NSTF based PEM electrolyzers, ECS Trans. 69 (2015) 893–917, https://doi.org/10.1149/06917.0893ecst.
[21] A. Bonakdarpour, et al., Oxygen reduction activity of Pt and Pt Mn Co electrocatalysts sputtered on nano-structured thin film support, Electrochim. Acta 53 (2007) 688–694.
[22] N.K. Oh, et al., Highly efficient and robust noble-metal free bifunctional water electrolysis catalyst achieved via complementary charge transfer, Nat. Commun. 12 (2021) 4606, https://doi.org/10.1038/s41467-021-24829-8.
[23] J. Zhang, et al., Core-shell nanostructured Ru@Ir–O electrocatalysts for superb oxygen evolution in acid, Small 18 (2022), 2108031, https://doi.org/10.1002/smll.202108031.
[24] F. Lv, et al., Iridium–tungsten alloy nanodendrites as pH-universal water-splitting electrocatalysts, ACS Cent. Sci. 4 (2018) 1244–1252, https://doi.org/10.1021/acscentsci.8b00426.
[25] J. Xu, et al., Atomic-step enriched ruthenium–iridium nanocrystals anchored homogeneously on MOF-derived support for efficient and stable oxygen evolution in acidic and neutral media, ACS Catal. 11 (2021) 3402–3413, https://doi.org/10.1021/acscatal.0c04117.

[26] D. Wu, et al., Efficient overall water splitting in acid with anisotropic metal nanosheets, Nat. Commun. 12 (2021) 1145, https://doi.org/10.1038/s41467-021-20956-4.
[27] M. Liu, et al., Ultrafine ruthenium–iridium–tellurium nanotubes for boosting overall water splitting in acidic media, J. Mater. Chem. A 10 (2022) 2021–2026, https://doi.org/10.1039/D1TA07789A.
[28] H. Guo, et al., Rational design of rhodium–iridium alloy nanoparticles as highly active catalysts for acidic oxygen evolution, ACS Nano 13 (2019) 13225–13234, https://doi.org/10.1021/acsnano.9b06244.
[29] S. Higashi, et al., Freestanding interconnected nanocluster textiles for efficient oxygen evolution reaction, J. Mater. Chem. A 8 (2020) 25061–25072, https://doi.org/10.1039/D0TA07707K.
[30] S. Higashi, T. Hirai, M. Matsubara, H. Yoshida, A. Beniya, Dynamic viscosity recovery of electrospinning solution for stabilizing elongated ultrafine polymer nanofiber by TEMPO-CNF, Sci. Rep. 10 (2020) 13427, https://doi.org/10.1038/s41598-020-69136-2.
[31] S. Higashi, T. Matsui, A. Beniya, Rapid solar heating of antimicrobial Ag and Cu2O nanostructured plasmonic textile for clean water production, ACS Appl. Mater. Interfaces (2022), https://doi.org/10.1021/acsami.2c09298.
[32] C. Rakousky, et al., An analysis of degradation phenomena in polymer electrolyte membrane water electrolysis, J. Power Sources 326 (2016) 120–128, https://doi.org/10.1016/j.jpowsour.2016.06.082.
[33] F. Godínez-Salomón, et al., Self-supported hydrous iridium–nickel oxide two-dimensional nanoframes for high activity oxygen evolution electrocatalysts, ACS Catal. 8 (2018) 10498–10520, https://doi.org/10.1021/acscatal.8b02171.
[34] D.F. Abbott, et al., Iridium oxide for the oxygen evolution reaction: correlation between particle size, morphology, and the surface hydroxo layer from operando XAS, Chem. Mater. 28 (2016) 6591–6604, https://doi.org/10.1021/acs.chemmater.6b02625.
[35] T. Reier, et al., Electrocatalytic oxygen evolution on iridium oxide: uncovering catalyst-substrate interactions and active iridium oxide species, J. Electrochem. Soc. 161 (2014) F876–F882, https://doi.org/10.1149/2.0411409jes.
[36] T. Reier, et al., Molecular insight in structure and activity of highly efficient, low-Ir Ir–Ni oxide catalysts for electrochemical water splitting (OER), J. Am. Chem. Soc. 137 (2015) 13031–13040, https://doi.org/10.1021/jacs.5b07788.
[37] H.G. Sanchez Casalongue, et al., In situ observation of surface species on iridium oxide nanoparticles during the oxygen evolution reaction, Angew. Chem. Int. Ed. 53 (2014) 7169–7172, https://doi.org/10.1002/anie.201402311.
[38] B. Ravel, M. Newville, Athena, Artemis, Hephaestus: data analysis for X-ray absorption spectroscopy using IFEFFIT, J. Synchrotron Radiat. 12 (2005) 537–541.
[39] H.N. Nong, et al., A unique oxygen ligand environment facilitates water oxidation in hole-doped IrNiOx core–shell electrocatalysts, Nat. Catal. 1 (2018) 841–851, https://doi.org/10.1038/s41929-018-0153-y.
[40] K.A. Lewinski, D. van der Vliet, S.M. Luopa, NSTF advances for PEM electrolysis-the effect of alloying on activity of NSTF electrolyzer catalysts and performance of NSTF based PEM electrolyzers, ECS Trans. 69 (2015) 893.
[41] S. Sun, Z. Shao, H. Yu, G. Li, B. Yi, Investigations on degradation of the long-term proton exchange membrane water electrolysis stack, J. Power Sources 267 (2014) 515–520, https://doi.org/10.1016/j.jpowsour.2014.05.117.
[42] F. Fouda-Onana, et al., Investigation on the degradation of MEAs for PEM water electrolysers part I: effects of testing conditions on MEA performances and membrane properties, Int. J. Hydrog. Energy 41 (2016) 16627–16636, https://doi.org/10.1016/j.ijhydene.2016.07.125.
[43] S. Siracusano, et al., New insights into the stability of a high performance nanostructured catalyst for sustainable water electrolysis, Nano Energy 40 (2017) 618–632, https://doi.org/10.1016/j.nanoen.2017.09.014.
[44] J. Kibsgaard, I. Chorkendorff, Considerations for the scaling-up of water splitting catalysts, Nat. Energy 4 (2019) 430–433, https://doi.org/10.1038/s41560-019-0407-1.
[45] O. Matz, M. Calatayud, Periodic DFT study of rutile IrO2: surface reactivity and catechol adsorption, J. Phys. Chem. C 121 (2017) 13135–13143, https://doi.org/10.1021/acs.jpcc.7b01990.
[46] J.J. Velasco-Vélez, et al., Electrochemically active Ir NPs on graphene for OER in acidic aqueous electrolyte investigated by in situ and ex situ spectroscopies, Surf. Sci. 681 (2019) 1–8, https://doi.org/10.1016/j.susc.2018.10.021.
[47] J. Mo, et al., Experimental studies on the effects of sheet resistance and wettability of catalyst layer on electro-catalytic activities for oxygen evolution reaction in proton exchange membrane electrolysis cells, Int. J. Hydrog. Energy 45 (2020) 26595–26603, https://doi.org/10.1016/j.ijhydene.2020.07.087.
[48] E. Willinger, C. Massué, R. Schlögl, M.G. Willinger, Identifying key structural features of IrOx water splitting catalysts, J. Am. Chem. Soc. 139 (2017) 12093–12101, https://doi.org/10.1021/jacs.7b07079.
[49] D. Li, et al., Highly quaternized polystyrene ionomers for high performance anion exchange membrane water electrolysers, Nat. Energy 5 (2020) 378–385, https://doi.org/10.1038/s41560-020-0577-x.
[50] Y.-R. Zheng, et al., Monitoring oxygen production on mass-selected iridium–tantalum oxide electrocatalysts, Nat. Energy (2021), https://doi.org/10.1038/s41560-021-00948-w.
[51] A. Li, et al., Enhancing the stability of cobalt spinel oxide towards sustainable oxygen evolution in acid, Nat. Catal. 5 (2022) 109–118, https://doi.org/10.1038/s41929-021-00732-9.
[52] M. Malinovic, M. Ledendecker, Whittling iridium down to size, Nat. Energy (2021), https://doi.org/10.1038/s41560-021-00963-x.